



LCRD OGS-1 Boundary Layer Scintillometer

Janet P. Wu, Preston Hooser, William Buehlman, and
Sabino Piazzolla

ABSTRACT

In May 2018, a boundary layer scintillometer (BLS) was deployed to monitor the optical turbulence in horizontal layer of the atmosphere in front the OCTL telescope at NASA/JPL's Table Mountain Facility. The instrument measures the path averaged coefficient of the structure function of the refractive index (C_n^2). The instrument is a BLS900 from Scintec AG. This document provides a documentation about the instrument deployment, the software, the theory related to the measurement of the C_n^2 and a first analysis of one year of data (May 2018 to June 2019). The boundary layer scintillometer is part of the atmospheric channel monitoring (ACM) system that is pertinent of the optical ground station 1 (OGS-1) of the LCRD mission

ACM REPORT

September 2019

Contents

<i>LCRD OGS-1 Boundary Layer Scintillometer</i>	0
1 Basic System Description	2
1.1 Hardware Layout	2
1.2 System Settings	3
2 Start Up Operation	4
2.1 Initiate SPU Connection	5
2.2 BLS900 Device Status	6
2.3 Device Time Maintenance	7
2.3 SPU Internal Memory Maintenance.....	8
2.5 (Optional) View Real-Time Data.....	9
2.6 (Optional) View Measurement Configuration	10
2.7 (Optional) View Hardware Configuration	12
3 Output Data File	13
4 Error Messages	15
5 BLS900 Scintec Specs	17
6 BLS900 Theory	21
7 Filtering of the data	26
7.1 Raw Data	26
7.2 First Filtering	28
7.3 Sun Zenith Angle dependence	29
7.4 Monthly Variation	33
8 Summary	40
9 References	40

1 Basic System Description

The BLS900 system emits pulsed 880-nm wavelength light towards a receiver along a near horizontal path relatively close to the surface. The measured signal intensity fluctuation at the receiver is used to derive the refractive index structure parameter (C_n^2) caused by atmospheric surface layer turbulence. Details of the methodology and instrument can be found in reference [1].

1.1 Hardware Layout

The hardware consists of a transmitter, receiver, and signal processing unit (SPU). The transmitter uses a total of 888 light emitting diodes (LED) on two disks (444 on each disc) to emit signals at a selectable pulse repetition rate. The receiver is located a known distance away, referred to here as the path length, to measure the transmitted signal intensity. A set of path reduction apertures may be placed on the front end of the transmitter and receiver to allow measurements across a relatively shorter separation distance down to a range between 250-m and 1-km. In the current BLS900 setup, path reduction apertures are not used while the transmitter is mounted on a tower approximately 24.4-m at Blue Ridge (located 3.46-km south of TMF) and the receiver resides on the OCTL roof. Figure 1 includes a geographical map identifying the transmitter and receiver locations. The receiver is connected to the SPU, which handles data acquisition and signal processing. A crossover Ethernet cable is used to connect the SPU directly to a computer. Figure 2 shows the hardware connection layout. Additional details on hardware specifications and transmitter/receiver alignment instructions can be found in the manufacturer installation manual given in reference [2].

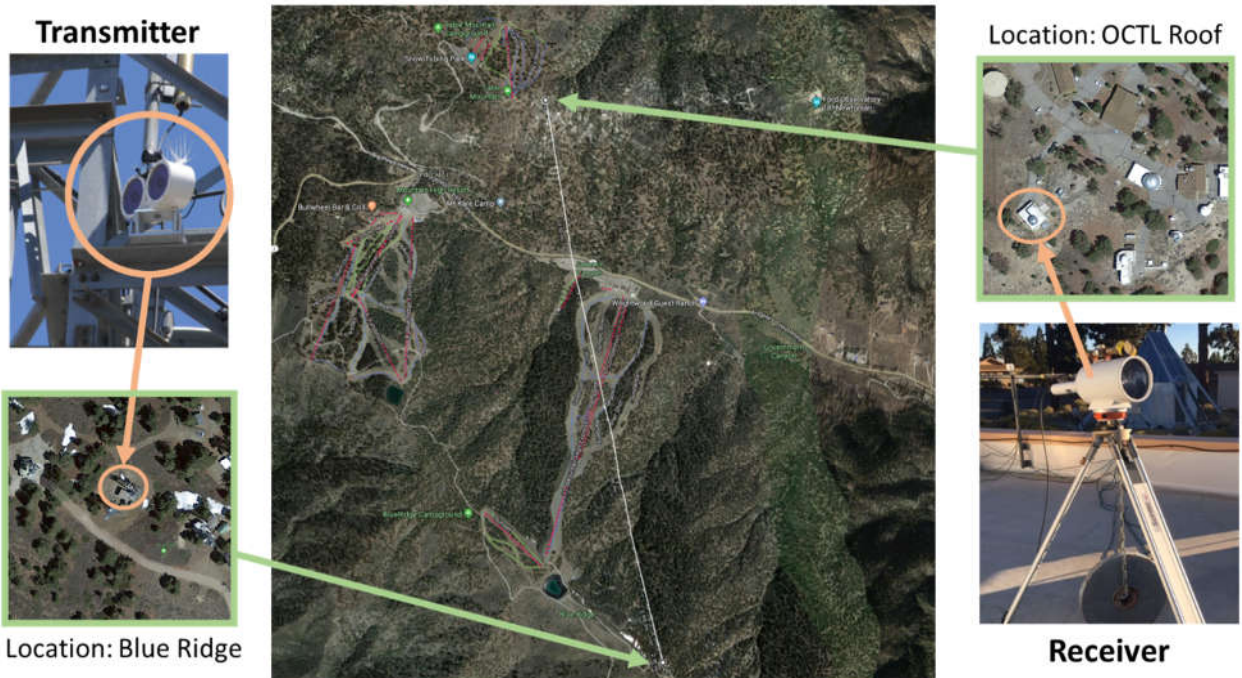


Figure 1: Transmitter and receiver geographical locations.

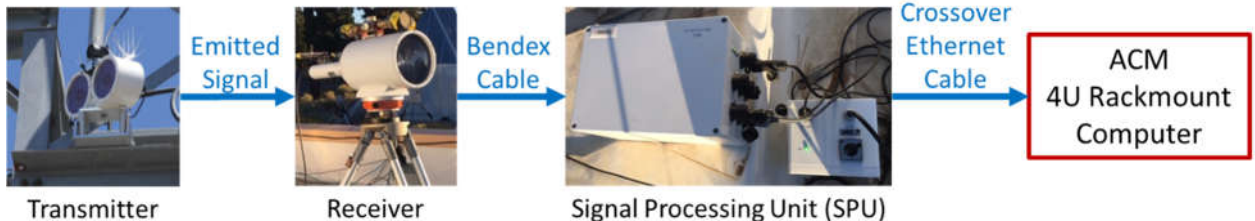


Figure 2: System hardware components and connections. The laser transmitter is mounted to a 24.4-m tower located 3.4-km south of TMF pointed towards the receiver on the OCTL roof. The receiver is connected to the SPU. A crossover Ethernet cable is used to directly connect the SPU to the data retrieval computer Ethernet port.

1.2 System Settings

This subsection pertains to specific system settings for the operational setup described above. These parameters should not be altered unless significant changes to the hardware setup are necessary. Table 1 lists the settings that require physical adjustments on the transmitter and receiver hardware. The user should refer to the manufacturer installation manual as a guide to selecting settings and locating the appropriate switches before attempting adjustments, especially

on the transmitter where there is very limited physical access to the tower. Table 2 lists the SPU system settings that are configured and synchronized through software, see section 2.

BLS900 Transmitter/Receiver Settings	
Transmitter Switches <ul style="list-style-type: none">➔ Pulse Repetition Rate➔ “Long Path”➔ “Boost”	25 Hz ON OFF
Receiver Dip Switches <ul style="list-style-type: none">➔ “1 & 5”➔ “2 & 6”➔ “3 & 7”➔ “4 & 8”	ON OFF OFF OFF

Table 1: Specific transmitter and receiver hardware settings for the BLS900 installation described in section 1.1. Transmitter pulse repetition rate is the emitted signal rate. The “long path” and “boost” switches are used to adjust transmitter power consumption to aid in prolonging LED lifetime. The receiver dip switches are used to adjust the receiver signal sensitivity to within an optimum range of detection values. The manufacturer installation manual provides recommended setting selection tables.

BLS900 SPU and Software Settings	
Device Connect <ul style="list-style-type: none">➔ Address (set by manufacturer)➔ Port 1 (use default)➔ Port 2 (use default)	SPU-112-151 10630 10631
Hardware Configuration <ul style="list-style-type: none">➔ BLS Model	Boundary Layer Scintillometer BLS900
Measurement Configuration <ul style="list-style-type: none">➔ Calculations and Measurements➔ Site Parameter – Path Length	Optical Turbulence Cn2 3.426 km
Measurement Configuration (Advanced) <ul style="list-style-type: none">➔ Averaging Period➔ Diagnosis Subperiod	1 minute 30 seconds

Table 2: Specific SPU and software settings for the BLS900 hardware installation described in section 1.1.

2 Start Up Operation

The manufacturer provided software called SRUN is the user interface to the SPU for data retrieval, adjusting configuration settings, monitoring instrument status, and changing operating

modes. This section is intended as a basic guide for software connection to the SPU, checking the system operating status, and low level maintenance. Advanced software configuration instructions specifically for forwarding data as required by LCRD Optical Ground Station (LOGS) operations are detailed in a separate document, reference [3]. The steps outlined in subsections 2.1 – 2.2 are required for startup. Subsections 2.3 – 2.4 are highly recommended additional steps to ensure data is saved. Optional steps to verify system settings are provided in subsections 2.5 – 2.7.

2.1 Initiate SPU Connection

The SPU connection and SRun installation is on the ACM computer connected to TMFnet IP 192.138.101.165 also identified as “octl-acm-3”. This computer runs on a Windows 7 (32-bit) operating system. To start the SRun software, click on the lower left corner Windows “Start” icon and navigate to All Programs → SRun 1.39 [folder] → SRun 1.39 [program] as shown in Figure 3. The SRun GUI will appear in a new window and a majority of it will be blank until a connection to the SPU is established. Click on the “Connect” button near the upper left corner of the SRun window (Figure 4). A new popup window will appear overlaid the main GUI. The IP address/network name set by the manufacturer is unique for each BLS system. Be sure all the device address parameters match what is shown in Figure 4. Next click on “Connect to Device”.

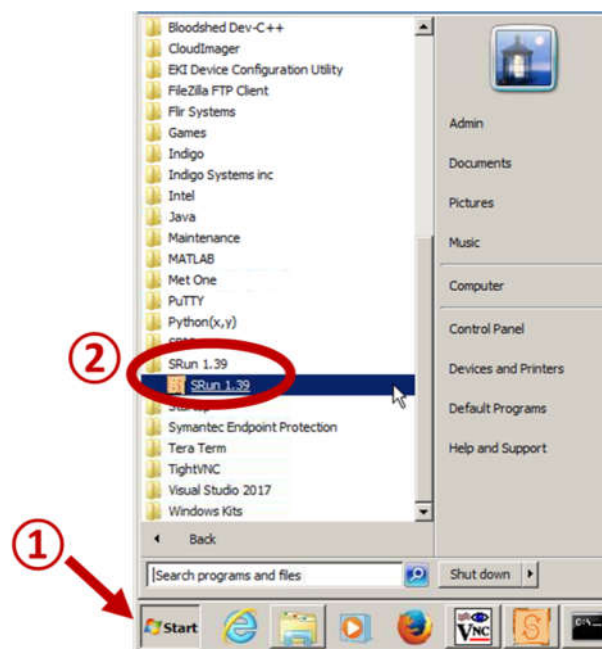


Figure 3: Start menu location to open SRun software.

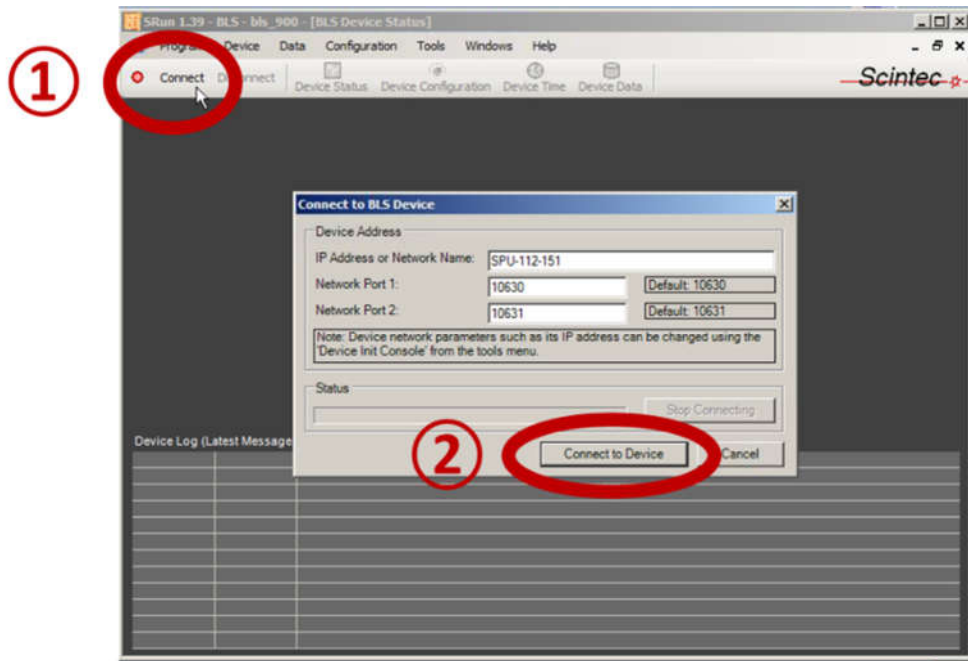


Figure 4: SRun window at software startup and initiating a connection to the SPU.

2.2 BLS900 Device Status

A successful software connection to the SPU will update the window to show an overview of the real-time operating status, such as Figure 5. This includes the received signal intensity values, general software activity, and errors/warnings such as misalignment. Refer to the comprehensive manufacturer software manual, reference [3], for the full list of possible messages and their meaning. If the signal plots and values are not shown on the right hand side of the window like in the figure below, check the measurements indicator (red highlighted circle in the figure). If the SPU is taking measurements, the button should show "Stop Measurement". If the button shows "Start Measurement", then click on that button to initiate the SPU to execute the measurement routine. The SPU normally repeats the measurement routine automatically even when not connected to the software unless there was a power loss to the SPU or the user had clicked on "Stop Measurement".

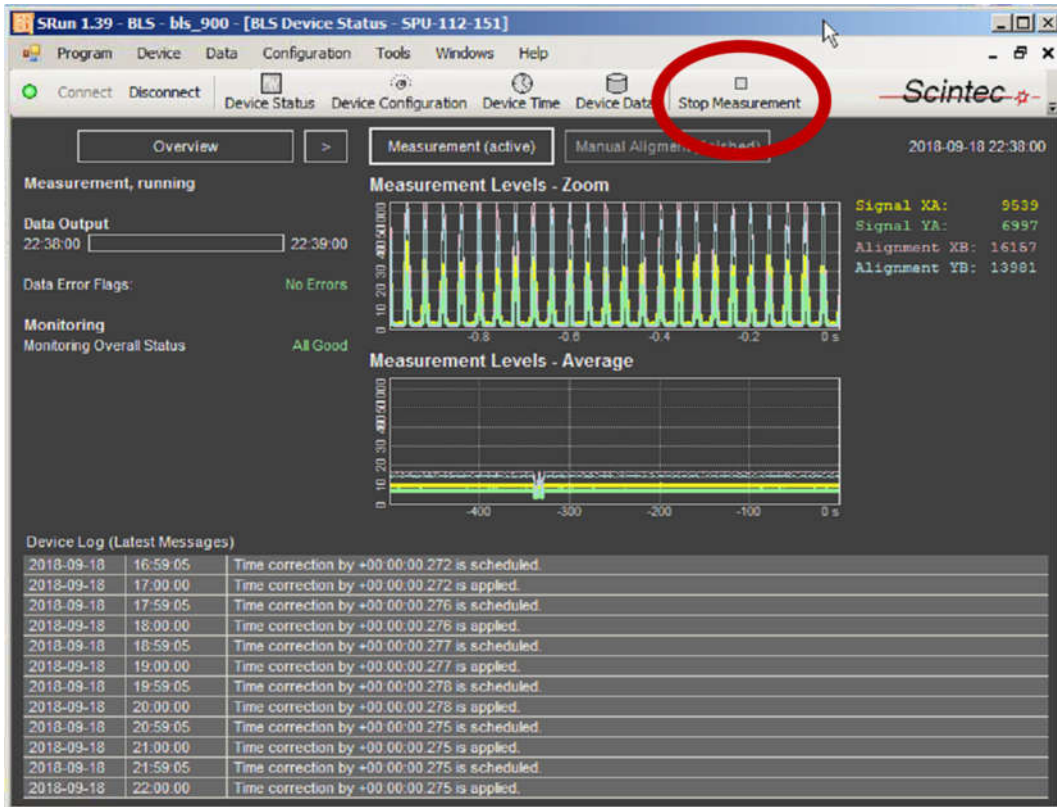


Figure 5: SRun window of the device operating status. Real-time received signal values, general log messages (up to 12 most recent), and any error messages are displayed here. The receiver outputs labeled XA and YA refer to the averaged receiver signal intensity values from each of the two light emitting transmitter disks. There are also two simultaneous alignment signals XB and YB that indicate how the transmitter and receiver are aligned.

2.3 Device Time Maintenance

The SPU internal clock has been observed to drift, which can lead to a relatively significant difference to the current time.

The SRun software setting for automated time correction is enabled for the current device to synchronize with a known time source every hour. However, the device log has consistently shown a time correction of more than 0.25 second was applied at each hourly synchronization. An example of these messages can be seen in Figure 5 where they are displayed in the log activity section located at the bottom half of the real-time status window.

Any loss of power to the SPU will reset the internal clock to a manufacturer default date and time. It is especially important for the user to check the displayed time located in the upper right corner of the real-time status window. Should a manual date/time update be needed, click on the "Device Time" button as shown in Figure 6. A new popup window will appear, then click on the

“Write Date and Time to Device” button to initiate synchronization. A successful update will show the corrected time difference. Click on the “Done” button to close the popup window.

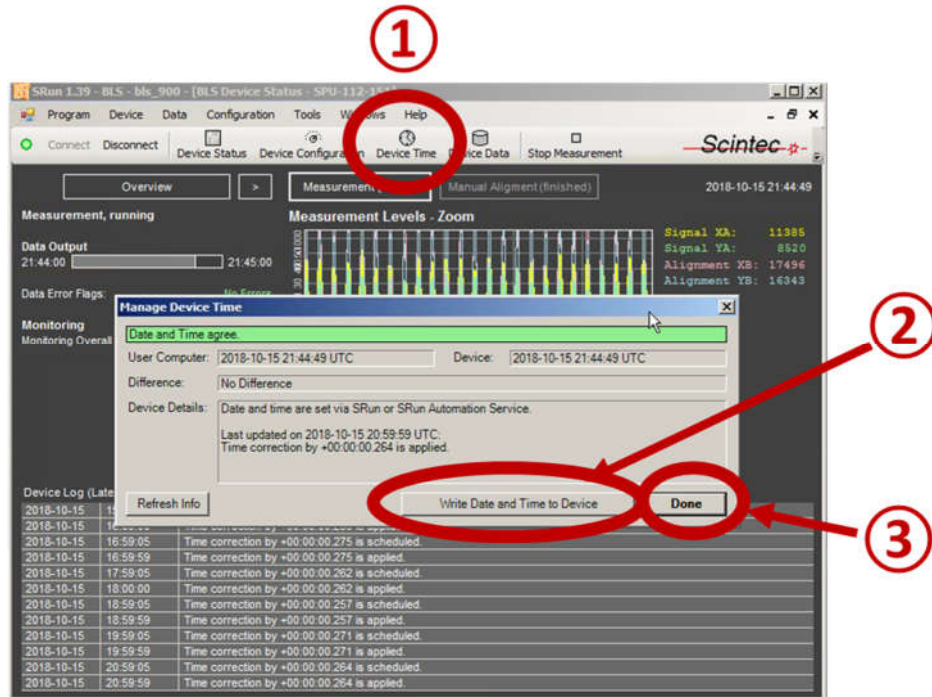


Figure 6: Device time synchronization display.

2.3 SPU Internal Memory Maintenance

The SPU repeatedly executes the measurement routine and stores all the measured and calculated data within internal memory, approximately 6 GB capacity. Older data will be overwritten if the memory becomes full. The user should regularly monitor how much remaining storage is available and it may become necessary to delete old files from the SPU device. Click on the “Device Data” button and a new popup window will appear with a list of all the stored data files (Figure 7). The list is synchronized with a designated data folder on the computer such that grayed out filenames indicate those particular files already exist in the folder, data file details are discussed in section 3. The top portion of the window will state how full the device is. If it is getting close to reaching maximum capacity, click on the “Retrieve and Clear Device” button to automatically download remaining new data onto the computer followed by automatic deletion of ALL files from the SPU internal memory. Push the “Done” button when the process has completed, which may take a few minutes depending on the total number of files to be downloaded and deleted.

Select “Actions” among the tabs in the properties window.

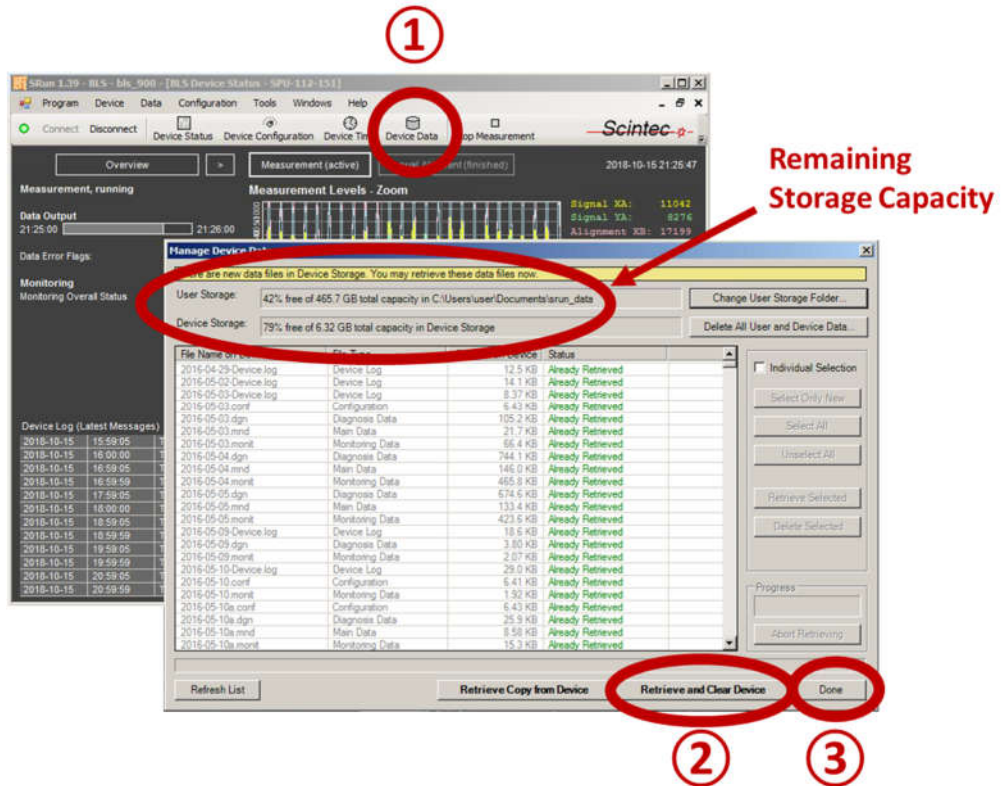


Figure 7: Viewing data file list stored in SPU internal memory.

2.5 (Optional) View Real-Time Data

The real-time computed refractive index structure parameter (C_n^2) values can be viewed by changing the main window display (Figure 8). From the toolbar menu, select Data → Show Main Data Table. This will switch the main view to show a table of the 10 most recent computed values and automatically refreshes when a new measurement is acquired. To return back to the view for device status overview, in the toolbar menu select Windows → BLS Device Status – SPU-112-151

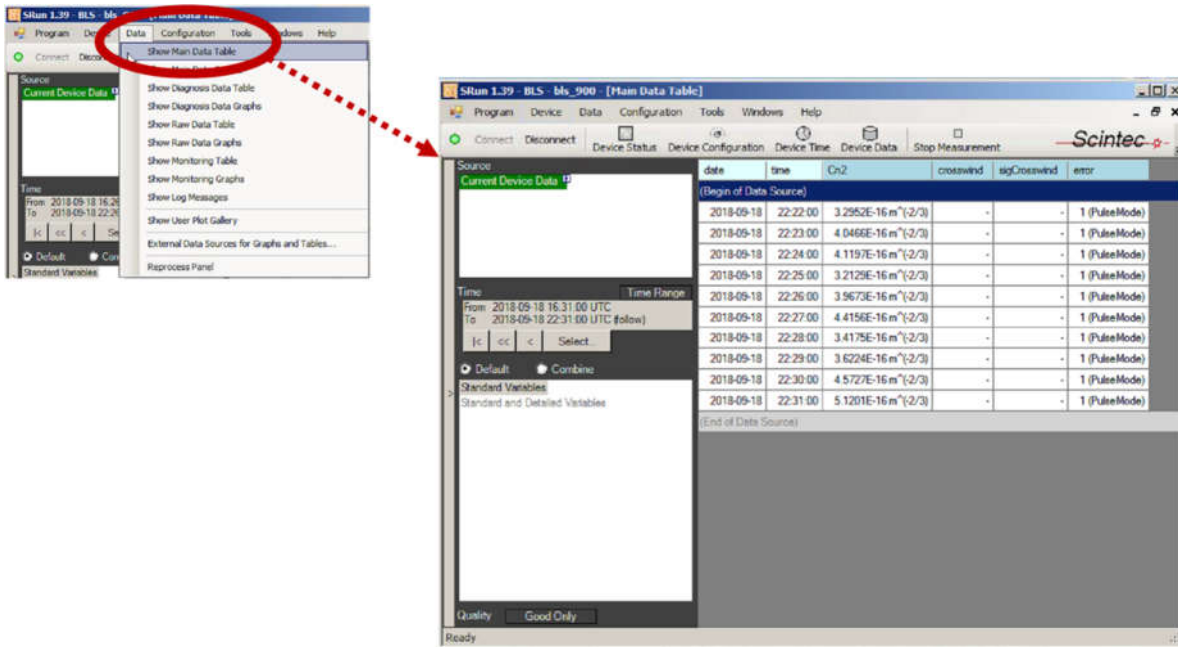


Figure 8: Main data table view with 10 most recent C_n^2 values.

2.6 (Optional) View Measurement Configuration

If needed, the user can verify the defined path length between the transmitter and receiver. From the toolbar menu, select Configuration → Measurement Configuration. A new popup window will appear where the path length parameter is specified as well as available calculation options (Figure 9). This window also provides access to verify the measurement averaging period and internal hardware self-test frequency by clicking on the “Advanced Configuration” tab (Figure 10). Both Figures 9 and 10 show the settings for the current BLS setup. If no changes are required, click the “Cancel” button on the popup window. To return back to the view for device status overview, in the toolbar menu select Windows → BLS Device Status – SPU-112-151. NOTE: If any updates were made to the configuration, the software and SPU do not automatically synchronize these changes and the user will need to manually upload them to the SPU. Mismatched configuration parameters may lead to unexpected results. Refer to the manufacturer system manual on how to synchronize configuration changes.

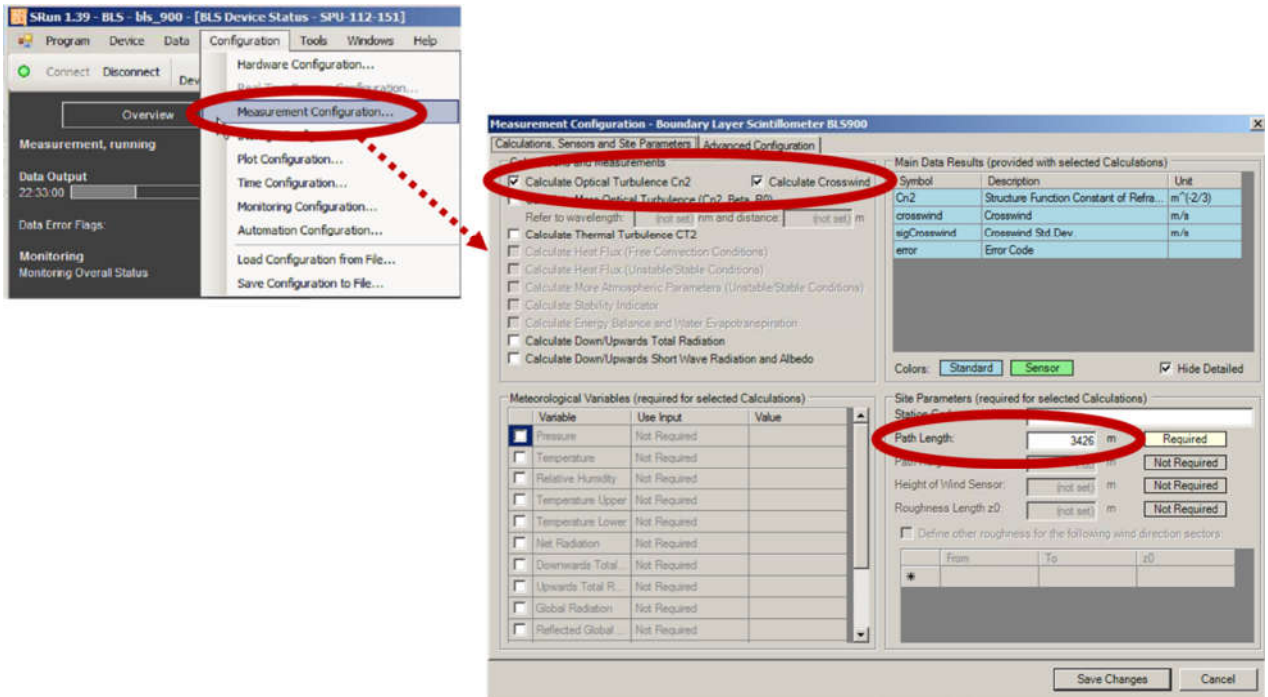


Figure 9: “Calculations, Sensors, and Site Parameters” tab view in the measurement configuration window to verify or update the transmitter/receiver path length and selectable calculation options.

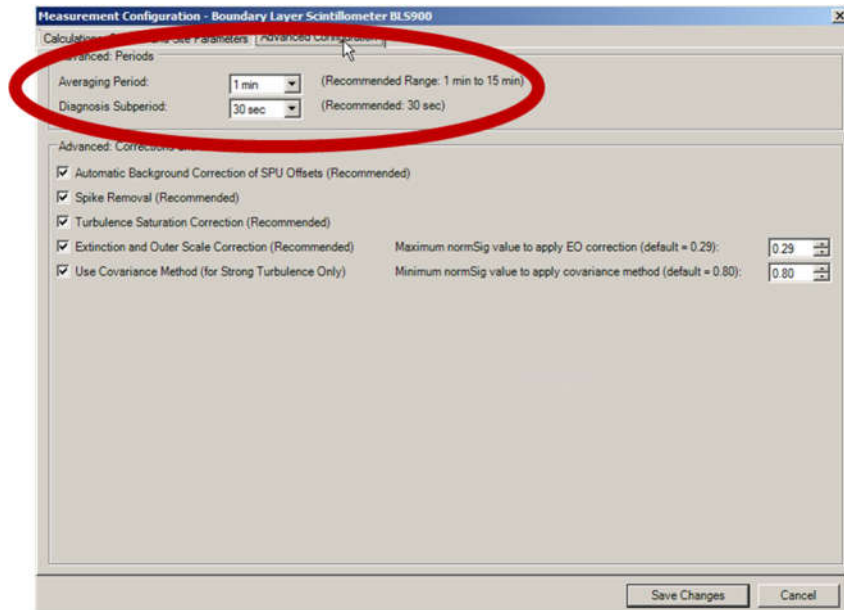


Figure 10: “Advanced Configuration” tab view in the measurement configuration window to verify or update the measurement averaging period and internal hardware self-test period.

2.7 (Optional) View Hardware Configuration

If the user needs to verify the hardware configuration, it can be viewed by selecting Configuration → Hardware Configuration in the toolbar menu. A new popup window will appear as shown in Figure 11, which are the settings for the current BLS setup. Click “Cancel” if no changes are required. As noted in the previous subsection, configuration changes are not automatically synchronized between the software and SPU. If changes are required, refer to the manufacturer system manual on how to synchronize configuration settings.

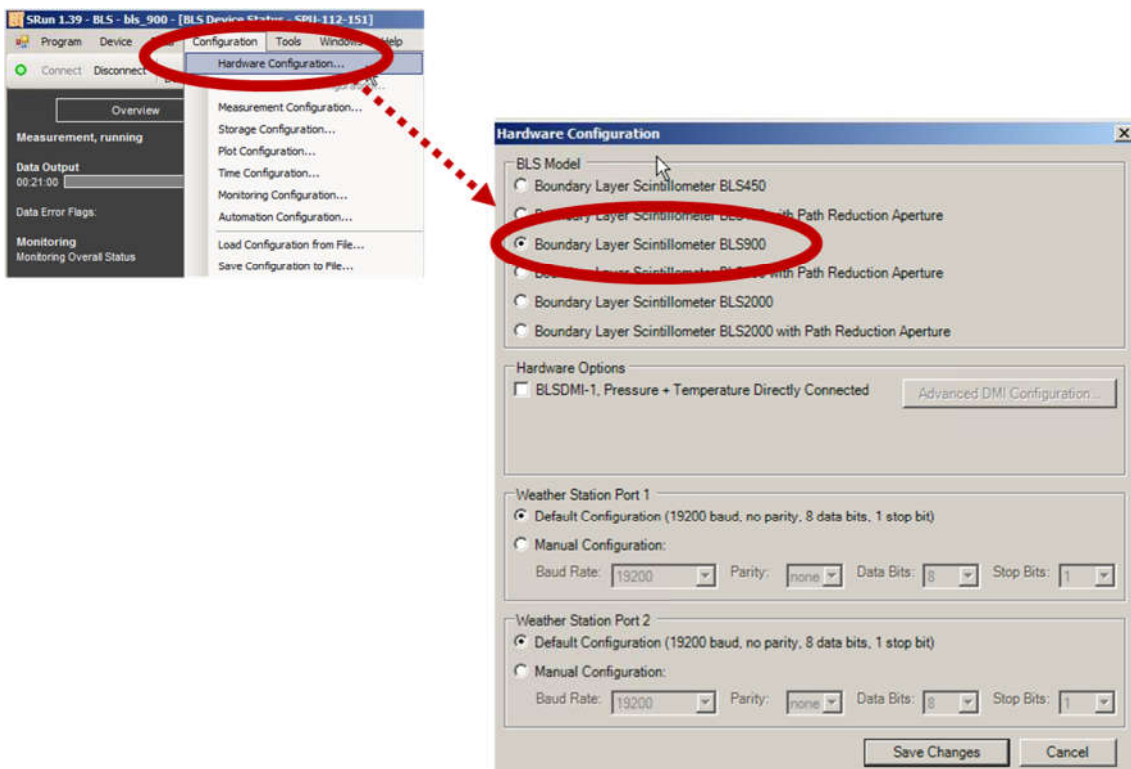


Figure 11: Hardware configuration display.

3 Output Data File

The SPU creates a set of files each day for every new UT date. The data contents of the collective daily file set include diagnostic, raw measurements, calculated results, hardware configuration settings, and device log messages. This section is limited to the measurement file only. Detailed descriptions of the content from other data files and error codes can be found in reference [3].

All data logger files are downloaded into a user specified ACM computer folder, currently C:\Users\user\Documents\srun_data. The data set file types are distinguished by the file extension name. The main measurement data files specifically have the *.mnd extension and filenames correspond to UT date with format <year> - <month> - <day>. The measured data and associated calculated results are tab delimited with the column ordering below.

In Fig. 12 there is a short excerpt from one of the .mnd files (header lines included). These data were edited to improve the reading the data in this figure example. In facts, the terms C1 to C19 (standing for Column 1 to Column 19) were introduced in the text. Each measurement record is a long string and is shown in the figure, next we briefly explain/comment the meaning of the different parameters presented from column 1 to column 19. A number of these parameters are related to the scintillometer theory [1], which is briefly described in Sec. 6.

- C1** Time # time # T3 # 1. Measurement time stamp. Interval is set to 60 s.
- C2** Structure Function Constant of Refractive Index Fluctuations at Instrument Wavelength # Cn2 # m^{-2/3}. This is the main parameter extracted by measurement, explained in Sec. 6.
- C3** Crosswind Wind measurements not available in this set up.
- C4** Crosswind Std.Dev. Wind measurements not available in this set up.
- C5** Path Length # pathLength # Tx to Rx range for the current set up.
- C6** Cn2 Extinction/Outer Scale Corrections. Correction for contribution outside the inertial range, see Sec. 6
- C7** Cn2 Saturation Correction Factor # correctCn2Sat # Correction for signal saturation, see Sec. 6.
- C8** Cn2 Covariance Correction Factor # Covariance of log-normal correction due to saturation, see Sec. 6.
- C9** Main Data Counter # mndCounter # # S # 1 # Counts.
- C10** Average XA (Corrected) # <XA>(c) Average counts in the signal from disc 1, see Sec. 6.
- C11** Average YA (Corrected) # <YA>(c) Average counts in the signal form disc 2, see Sec. 6.
- C12** Normalized Std.Dev. XA (Corrected). Scintillation index from disc 1 signal.
- C13** Normalized Std.Dev. YA (Corrected); Scintillation index from disc 2 signal.
- C14** Correlation XA/YA (Corrected). Correlation Coefficient between signals from the two discs.
- C15** Number of Valid Diagnosis Subperiods; Diagnostic;
- C16** Number of Valid Diagnosis Subperiods for Crosswind. No present in actual setup.
- C17** Total Number of Diagnosis Subperiods; Diagnostic;
- C18** Combined Channel Flags ; Diagnostic message;
- C19** Error Code # error # ; Diagnostic message.

Measurement Record from BLS900																		
C1	C2	C3	C4	C5	C6	C7	C8	C9	C10	C11	C12	C13	C14	C15	C16	C17	C18	C19
PT08H00555 / 2019-01-04T00:01:00Z	3.1730E-15	N/A	N/A	3426	0.912	1.089	N/A	123798	22136.1	16642.9	0.832643	0.834316	0.178	2	0	2	0	1
PT08H00555 / 2019-01-04T00:02:00Z	3.2934E-15	N/A	N/A	3426	0.884	1.089	N/A	123799	22186.6	16753.7	0.8334669	0.8343631	0.283	2	0	2	0	1
PT08H00555 / 2019-01-04T00:03:00Z	3.4164E-15	N/A	N/A	3426	0.793	1.089	N/A	123800	22186.6	16662.6	0.8336178	0.8338722	0.285	2	0	2	0	1
PT08H00555 / 2019-01-04T00:04:00Z	2.2283E-15	N/A	N/A	3426	0.889	1.088	N/A	123801	22186.7	16725.4	0.8328827	0.8338763	0.271	2	0	2	0	1
PT08H00555 / 2019-01-04T00:05:00Z	1.4119E-15	N/A	N/A	3426	0.788	1.086	N/A	123802	22186.7	16669.3	0.8323789	0.8324529	0.297	2	0	2	0	1
PT08H00555 / 2019-01-04T00:06:00Z	1.7387E-15	N/A	N/A	3426	0.831	1.086	N/A	123803	22148.9	16654.4	0.8250571	0.8265393	0.251	2	0	2	0	1
PT08H00555 / 2019-01-04T00:07:00Z	2.2844E-15	N/A	N/A	3426	0.828	1.086	N/A	123804	22247.3	16661.0	0.8225971	0.8225862	0.261	2	0	2	0	1
PT08H00555 / 2019-01-04T00:08:00Z	1.5716E-15	N/A	N/A	3426	0.812	1.088	N/A	123805	22137.7	16769.9	0.8224530	0.822538	0.268	2	0	2	0	1
PT08H00555 / 2019-01-04T00:09:00Z	2.2183E-15	N/A	N/A	3426	0.819	1.087	N/A	123806	22194.4	16761.8	0.8211110	0.821851	0.262	2	0	2	0	1
PT08H00555 / 2019-01-04T00:10:00Z	1.4980E-15	N/A	N/A	3426	0.911	1.088	N/A	123807	22175.2	16766.9	0.8226564	0.8232396	0.179	2	0	2	0	1
PT08H00555 / 2019-01-04T00:11:00Z	1.6344E-15	N/A	N/A	3426	0.955	1.088	N/A	123808	22191.4	16674.7	0.8222719	0.8232396	0.139	2	0	2	0	1
PT08H00555 / 2019-01-04T00:12:00Z	1.7565E-15	N/A	N/A	3426	0.744	1.088	N/A	123809	22173.9	16654.4	0.8202710	0.8202887	0.329	2	0	2	0	1
PT08H00555 / 2019-01-04T00:13:00Z	2.8079E-15	N/A	N/A	3426	0.814	1.088	N/A	123810	22155.2	16651.4	0.8205937	0.8205937	0.395	2	0	2	0	1
PT08H00555 / 2019-01-04T00:14:00Z	2.0293E-15	N/A	N/A	3426	0.954	1.088	N/A	123811	22172.1	16661.7	0.8225014	0.8227654	0.111	2	0	2	0	1
PT08H00555 / 2019-01-04T00:15:00Z	1.8208E-15	N/A	N/A	3426	0.897	1.088	N/A	123812	22148.9	16682.1	0.8225184	0.8226019	0.191	2	0	2	0	1
PT08H00555 / 2019-01-04T00:16:00Z	2.7693E-15	N/A	N/A	3426	0.964	1.089	N/A	123813	22183.2	16542.2	0.8291123	0.8313687	0.131	2	0	2	0	1
PT08H00555 / 2019-01-04T00:17:00Z	2.7228E-15	N/A	N/A	3426	0.991	1.089	N/A	123814	22287.6	16632.2	0.829688	0.8289466	0.187	2	0	2	0	1
PT08H00555 / 2019-01-04T00:18:00Z	2.8422E-15	N/A	N/A	3426	0.884	1.089	N/A	123815	22159.7	16657.5	0.8297788	0.834287	0.221	2	0	2	0	1
PT08H00555 / 2019-01-04T00:19:00Z	2.6802E-15	N/A	N/A	3426	0.987	1.088	N/A	123816	22159.7	16657.5	0.8297788	0.8318022	0.182	2	0	2	0	1

Figure 12. Measurement record from BLS900. Notice that the terms C1 to C19 (i.e. Column 1 to Column 19) were intentionally added in the text to improve the data interpretation

4 Error Messages

SRUN produces during the measurements a number of flag and (possible) error messages to diagnostic the quality of the link. The error messages are in any data sets (Raw data, main data, etc.) The error messages are listed below. One should ignore those relevant to the SLS system (yellow box), because belong to a different kind of scintillometer. The tables below are extracted from Ref. [1].

Error Code	Meaning
0	<i>No error or warning</i>
1 (SLS)	<i>Reserved</i>
1 (BLS)	<i>PulseMode</i> It was detected that the BLS transmitter was operated in non-continuous pulse mode. The pulses were automatically detected and signal processing was adapted accordingly. This code possesses informational character, only. This code may also occur when the received signal intensity is very low.
2	<i>Reserved</i>
4	<i>Reserved</i>
8	<i>Reserved</i>
16	<i>NoSignal</i> The received average intensity has dropped to a very low value. If there is no fog or obscuration, check alignment of receiver, alignment of transmitter and transmitter power.
32 (SLS)	<i>SignalReduced</i> The received average intensity has dropped to a value which is very much lower than at an earlier time of the measurement. If there is no fog or obscuration, check alignment, transparency of windows, transmitter power and pinhole adjustment.
32 (BLS)	<i>Misalignment</i> If this code occurs repeatedly and there is no fog or obscuration, the receiver should be re-aligned.
64	<i>SignalTooHigh</i> The <i>SignalTooHigh</i> Diagnosis Data warning flag was set in some of the processed Diagnosis Data sets. Input signals were too high and exceeded the available A/D range. A numerical correction was automatically applied to the results. Accuracy is reduced. If this warning code occurs repeatedly, you should reduce signal levels by adjusting the amplifier dip switch setting in the receiver, install Path Reduction Apertures (BLS only) or increase the path length.
128	<i>Reserved</i>
256	<i>ManyDgnInvalid</i> At least 50% of the Diagnosis Data sets were disregarded due to some warnings or errors. Check the respective dgnFlags for details on the reason of rejection.
512	<i>AllDgnInvalid</i> All Diagnosis Data sets were disregarded due to some warnings or errors. Check the respective dgnFlags for details on the reason of rejection.
1024	<i>Cn2Saturation</i> The measured fluctuations were too high and reached the saturation range (limit of weak scattering theory). In the case of BLS an automatic saturation correction is

Error Code	Meaning
	applied and this code is only set if the necessary corrections are too large. In this case the output results are not accurate. If this error code occurs repeatedly, you should choose a different measurement path with either reduced path length or with an increased path height to avoid saturation.
2048	<i>Cn2CorrectionFailed</i> An automatic correction that was applied to turbulence results has failed. The given result is based on uncorrected values, instead.
4096	<i>Reserved</i>
8192	<i>SomeMndlInvalid</i> Some Main Data results could not be calculated and were invalidated.
16384	<i>Configuration</i> Some outputs could not be calculated due to invalid, missing or inconsistent configuration parameters. If this code occurs, please check carefully your hardware and measurement configuration.
32768	<i>Sensor</i> Some outputs could not be calculated due to invalid or missing meteorological input data.
65536	<i>Monitoring</i> Built-in hardware monitoring indicates a power failure or hardware malfunction.
131072	<i>Background</i> An automatic background measurement failed, possibly due to hardware malfunction.
262144	<i>DMI</i> A DMI sensor (Direct Meteorological Input) provided invalid results. Check proper sensor configuration, cable connection and sensor setup.
524288	<i>WSP</i> An error occurred when reading sensor data from a Weather Station Port. Check configuration, cable connection and the connected equipment.
1048576	<i>Acquisition</i> An acquisition error occurred during sampling. The respective output has been invalidated.
2097152	<i>Reserved</i>
4194304	<i>Computation</i> A computation error occurred. The respective output has been invalidated.
8388608	<i>Reserved</i>
16777216	<i>UnidentifiedWarning</i> This flag only occurs if data is loaded or reprocessed that was originally recorded with a different software version. It indicates a warning flag that is not understood by this software version. This code exists solely for compatibility reasons.
33554432	<i>UnidentifiedError</i> This flag only occurs if data is loaded or reprocessed that was originally recorded with a different software version. It indicates an error flag that is not understood by this software version. This code exists solely for compatibility reasons.

Table 5. BLS900 error messages.

5 BLS900 Scintec Specs

The BLS900 consists of two transmitter discs emitting at 880nm and a receiver aperture of 14cm. Each transmitter disc consist of 444 LED emitters, the overall transmitted signal has a beam width of 16°, which is relatively broad and allow an easy alignment with the receiver. The field of view of the receiver is 8mrad. It is important to notice that each emitter disc modulates its own signal at a different frequency; this modulation diversity allows detection and separation of the signal coming from disc 1 and disc 2 at the emitter. Main characteristics of the BLS900 are summarized next in a booklet from Scintec; additional data in Table 1 (for the transmitter) and Table 2 (for the receiver) are extracted from the Scintec Hardware Manual [2].

BLS900

Large Aperture Scintillometer – Dual-Disk Design



Photo courtesy of CSIRO, South Africa

The Scintec BLS900 Large Aperture Scintillometer measures atmospheric turbulence, heat flux and crosswind over path lengths between 250 m and 6000 m. As part of a meteorological station it can also be used to determine the evapotranspiration over extended areas.

A scintillometer senses turbulence between an optical transmitter and a receiver. The operation principle is based on the modulation of light by atmospheric refractive index fluctuations in the air. The phenomenon is called scintillation and is the reason why stars twinkle at night.

Compared to conventional turbulence measurements with point sensors, scintillometers gather spatially representative results with lower statistical scatter and shorter averaging times.

The Dual-Disk Design of the BLS900 provides for instantaneous corrections of absorption fluctuations, saturation of scintillation and outer scale effects. This results in significantly higher data quality and increased measurement ranges. All BLS Series scintillometers use LED arrays. Wide emission angles virtually eliminate the need for transmitter alignment and maintain high data accuracy even when used on towers which are prone to vibration.

Features

- measures turbulence over large spatial scales
- Dual-Disk Design for unrivalled accuracy
- crosswind measurement capability
- maximum path length 6000 m
- LED array eases transmitter alignment
- LED array allows transmitter to be mounted on vibrating towers
- built-in Receiver Alignment Monitor
- Signal Processing Unit performs all calculations
- 6 GB built-in data storage
- remote access
- infrared window heating available

Applications

- surface energy balance
- satellite data ground truth
- plant evapotranspiration
- agrometeorology, forestry
- hydrology, water management
- turbulence studies
- atmospheric dispersion
- optical propagation conditions
- defence weather
- runway crosswind

Data output		
Description	Specifications	Remarks
Data output includes (but is not limited to):		
<ul style="list-style-type: none"> ▪ structure parameter of refractive index fluctuations (C_n^2) ▪ structure parameter of temperature fluctuations (C_T^2) ▪ sensible heat flux 	<ul style="list-style-type: none"> ▪ crosswind (horizontal wind component perpendicular to the optical propagation path) ▪ mean, standard deviation, minimum and maximum of intensity (for each disk) ▪ scintillation index (at user-defined wavelength and path length) 	<ul style="list-style-type: none"> ▪ Fried diameter (at user-defined wavelength and path length) ▪ correlation coefficient of intensity ▪ raw intensity data (for each disk) ▪ data quality code
No. of transmitting disks	2	horizontally spaced
No. of LEDs	888 / 36	infrared / visible
Optical output power	15 W peak	at 880 nm wavelength
Transmitter divergence	16°	full width at half maximum
Receiver field of view	8 mrad	receiver alignment automatically monitored
Corrections for absorption fluctuations and outer scale effect	yes	automatic
Crosswind measurement capability	yes	in continuous mode only
Path length	100 / 500 to 6000 m	with / without Path Reduction Aperture
Pulse repetition rates	1, 5, 25 Hz or continuous	
Integration time	1 sec to 60 min	
Output ports	Ethernet, RS-232, analogue	ASCII
Data Storage Capacity	6 GB	
Internal clock	date and time	
Operating voltage	10 to 15 VDC	AC power supply available
Power consumption: Transmitter "Long Path", "Boost"	60 W / 14 W / 4 W / 2 W	continuous mode / 25 Hz / 5 Hz / 1 Hz pulse repetition rate
Power consumption: Receiver and SPU	16 W	
Operating temperature	-35 to +50°C (-30 to +120°F)	
Dimensions and weight: Transmitter	36 x 18 x 14 cm / 8.5 kg	
Dimensions and weight: Receiver	61 x 32 x 16 cm / 7.6 kg	
Dimensions and weight: SPU	33 x 23 x 18 cm / 8 kg	

Specifications	BLS450	BLS900	BLS2000	Remarks
Main radiation source	444 LEDs GaAlAs	888 LEDs GaAlAs	1756 LEDs GaAlAs	Infrared
Auxiliary radiation source	18 LEDs visible	36 LEDs	68 LEDs	Red
Maximal optical power	7.5 W	15 W	28 W	
Wavelength	880 nm	880 nm	880 nm	$\Delta\lambda = \pm 20 \text{ nm}$
Beam Divergence	16°	16°	16°	Full width half max
Pulse modes	slow, medium, fast, continuous	slow, medium, fast, continuous	slow, medium, fast, continuous	Approx. pulse rates for slow/medium/fast: 1 Hz/5 Hz/25 Hz.
Pulse length	8 ms	8 ms	8 ms	
Modulation frequency	1750 Hz	1750 Hz and 2500 Hz	1750 Hz and 2500 Hz	
Operation voltage	12 VDC	12 VDC	12 VDC	Max. Voltage 15 VDC
Power consumption "Long Path", "Boost"	2 W 4 W 7 W 30 W	2 W 4 W 14 W 60 W	4 W 12 W 36 W 156 W	At pulse mode: slow medium fast continuous
Dimensions	180 x 180 x 135 mm	364 x 180 x 135 mm	590 x 330 x 170 mm	
Weight	4.5 kg	8.5 kg	22 kg	

Table 3. Transmitter Specifications for the BLS900

Specifications	BLS450 and BLS900	BLS2000	Remarks
Lens	Plan convex	Fresnel, plan	
Focal length	450 mm	495 mm	
Diameter	140 mm	265 mm	
Field of view	8 mrad	7.5 mrad	
Detectors	2 Si Photodiodes	2 Si Photodiodes	
Sensitive area	15 mm ²	15 mm ²	Signal 1
Sensitive area	5 mm ²	5 mm ²	Signal 2
Dimension	Ø160 x 590 mm	570 x 480 x 300 mm	
Weight	7.6 kg	19 kg	

Table 4. Receiver Specifications for the BLS900

6 BLS900 Theory

In this section, we concisely describe the theory supporting the measure of the BLS900. Most of the theory in this section, it is derived from the BLS900 Theory Manual [1].

The BLS900 measures the path-averaged coefficient of the structure function of the refractive index between the two transmitters and the receiver.

The coefficient of the structure function of the refractive index, or Cn2, is a measure to the strength of the optical turbulence, and it is defined as

$$D_n(n(\mathbf{R})) = \langle [n(\mathbf{R}_1) - n(\mathbf{R}_2)]^2 \rangle = \langle [n(\mathbf{R}_1) - n(\mathbf{R}_1 + \mathbf{R})]^2 \rangle = C_n^2 R^{2/3}; \quad l_o < R < L_o, \quad (6.1)$$

in which D_n is the structure function of the refractive index n , and the symbol $\langle \rangle$ is the averaging operator. The randomness of the refractive index is mainly due to temperature fluctuations, and it is the source of the degradations that affect a propagating electromagnetic beam. The variable R in the Eq. 6.1 is the distance between the two points in space \mathbf{R}_1 and \mathbf{R}_2 . In Eq. 6.1, it is assumed that atmosphere is an isotropic medium, and the expression is valid if R is within an inertial range defined by the sizes of the ‘eddies’ L_o and l_o . The inertial range defines the region where the energy in air is transferred from large size ‘eddies’ to smaller sizes eddies up to those of smallest size l_o [6].

The Cn2 parameter is related to the three dimensional spectrum of the refractive index that can be expressed by the modified Kolmogorov spectrum [6] as

$$\Phi_n(\kappa, h) = 0.033 C_n^2(h) \frac{\exp(-\kappa^2 / \kappa_m^2)}{(\kappa^2 + \kappa_0^2)^{11/6}}, \quad 0 \leq \kappa < \infty, \quad (6.2)$$

where $\kappa_m = 5.92/l_o$ and $\kappa_0 = 1/L_o$, and κ is the inverse of the eddy size. The modified von Karman spectrum depicted in Fig. 6.1 .

The randomness of the refractive index degrades an electromagnetic beam propagating in turbulent medium in a number of ways. At the same time, the magnitude of Cn2 coefficient, among other things, is related to the fading the signal experiences (signal scintillation). Particularly, the BLS900 measures the fading of the propagating two beam emitted by the two transmitter discs, elaborates the statistics of the fading and then derives the path averaged Cn2. To understand how the instrument works one can start form the Maxwell’s equations as

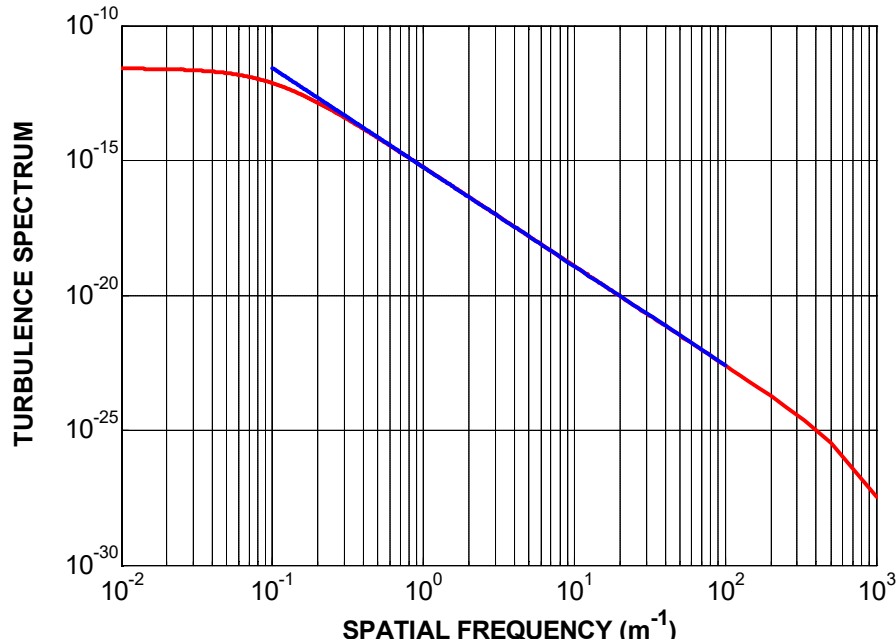


Figure 6.1. Modified spectrum of the refractive index. Notice that $C_n^2=10^{-13}$ while the actual sub inertial range is between 10 cm and 10 m (blue slope).

$$\nabla^2 E + k^2 n^2 E = 0, \quad (6.3)$$

where E is a scalar component of the electric field, and because here the refractive index is random variable, Eq. 6.3 is a stochastics differential equation.

A number of approaches have been considered to solve Eq. 6.3, among those, one of the best known is the Rytov method [6], which holds interesting and practical consequences for the characterization of the wave propagation in a random media.

According to the Rytov method, one first describes the scalar field as the complex exponential form

$$E = \exp(\psi), \quad (6.4)$$

with $\psi=\log(E)$. Then, rewriting the scalar Maxwell equation in term of the exponential term ψ one get the Riccati equation

$$\nabla^2 \psi + \nabla \psi \cdot \nabla \psi + k^2 n^2 = 0. \quad (6.5)$$

Close solution of the above equation is not obtainable, however, using the perturbation expansion of the electric field one can write

$$E = E_o + E_1 \cdot = \exp(\psi_o + \psi_1) \quad (6.6)$$

where E_o is the incident field and E_1 is the small field perturbation related to the first order scattering of the field with $|E_1| \ll |E_o|$, and ψ_1 is an exponential term related to E_1 . Of course, E_o and ψ_o are the solutions of the equation without perturbation. As consequence of Eq. 6.6 , one can write the exponential turbulence term as

$$\psi_1 = \psi - \psi_o = \log\left(\frac{|E|}{|E_o|}\right) + j(\phi - \phi_o) = \chi + jS \quad (6.7)$$

where χ is defined as the field log-amplitude, and S the field phase fluctuations.

Statistical measures of the log-amplitude χ are elaborated by the BLS900 and from those and $Cn2$ values are determined.

The BLS900 measures the signal intensities, I_1 and I_2 , originated by the transmitter disc 1 and disc 2. The instrument's signal processing unit (SPU) elaborates the statistics of the signals over a given interval of time (for the OGS-instrument this interval of time is set to 1 minute) with a sampling rate of 500 Hz. Particularly, the SPU is able to elaborate the following parameters:

- 1) Average Irradiance: $\langle I_1 \rangle, \langle I_2 \rangle$;
- 2) Standard deviation of the Irradiance: σ_1, σ_2 ;
- 3) Variance(s) of the log-amplitude of the signals [6] given by

$$B_{11} = \frac{1}{4} \log\left(1 + \left(\frac{\sigma_1}{\langle I_1 \rangle}\right)^2\right), \text{ for the disc 1 (6.8)};$$

$$B_{22} = \frac{1}{4} \log\left(1 + \left(\frac{\sigma_2}{\langle I_2 \rangle}\right)^2\right), \text{ for the disc 2 (6.9);}$$

- 4) The covariance of the log-normal amplitude between the two signals instead is

$$B_{12} = \frac{1}{4} \log\left(1 + \rho \left(\sqrt{1 + \left(\frac{\sigma_1}{\langle I_1 \rangle}\right)^2} \right) \left(\sqrt{1 + \left(\frac{\sigma_2}{\langle I_2 \rangle}\right)^2} \right)\right), \quad (6.10);$$

where ρ is the measured correlation coefficient between the two signals.

Once the SPU of the BLS900 derives the quantities above, it compares with the values derived from the theory and extract the path averaged $Cn2$ (explained later).

The receiving aperture of the BLS900 has a diameter $D = 14$ cm. The size of the receiving aperture implies that fading of the signal is mitigated by the aperture size (aperture averaging), and theory [7, 8] indicates that for the BLS900 the log-normal variance is related to the $Cn2$ as

$$B_{11} = B_{22} = (B_{11} + B_{22})/2 = 0.223 C_n^2 L^3 D^{-7/3}, \quad (6.11)$$

where L is the transmitter-to-receiver range.

When the range L and the $Cn2$ value increases so does the variance of the log-normal amplitude, Eq. 6.11, however, despite the aperture averaging effect of the receiver disc size of the BLS900, signal fading tends to saturate when the product $Cn2L^3$ is relatively large and corrections are necessary when deriving the correct log-normal variance from the measurements. Saturation is mainly due to optical turbulence transition from single scattering of the signal (weak turbulence) to multiple scattering (strong turbulence) along the path. Figure 6.2 illustrates how the signal saturation effect the log-normal variance in the BLS900. The dashed curve describe the B_{11} according to the weak scattering theory, while the saturating curves are the measured values at different values of $Cn2L^3$. For lower values of $Cn2L^3$, B_{11} is well predicted by the theory, Eq. 6.11. As the product $Cn2L^3$ increases, the measured values deviates from the weak scattering theory and tends to saturates. Fading saturation is monitored by the instrument SPU's and the proper correction are applied when the $Cn2$ is derived.

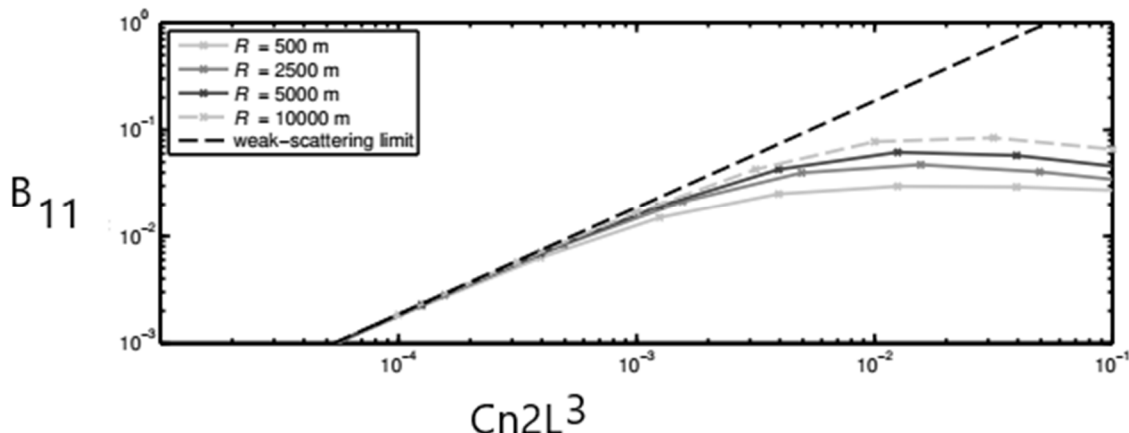


Figure 6.2 Effect of saturation on the variance of the signal lognormal for the BLS900

In the BLS900 system, noise and large signal absorption can affect also signal variance and covariance measurements, and its derivation of $Cn2$. To reduce noise and signal fluctuations that may originate by the vibration of the transmitters and may affect measurements of the path averaged $Cn2$, the BLS900 evaluates the Q quantity defined as [9]

$$Q = \frac{B_{11} - B_{22}}{2} - B_{12}, \quad (6.11)$$

One should notice now that the term Q is exempt from common fading of the signal from the two transmitting discs, while the information about the optical turbulence collected by B11, B12 and B12 is preserved. The BLS900 derives Cn^2 from Q as

$$C_n^2 = \frac{\alpha_{11}}{(1 - \frac{\alpha_{11}}{\alpha_{12}})} L^{-3} Q, \quad (6.12)$$

where for the deployed system we have $\alpha_{11}=0.4940E-2$, and $\alpha_{12}=0.5$ [1].

In essence, to measure the path average Cn^2 over a range L between the two discs of the transmitter and the receiver, the BLS900 performs the following steps:

- 1) Set an observation time ΔT (for OGS-1 operation $\Delta T = 60$ s);
- 2) Record time series of signal intensity from disc 1 I_1 over the interval ΔT ;
- 3) Record time series of signal intensity from disc 2 I_2 over the interval ΔT ;
- 4) SPU calculates the log-normal variance from disc 1, B_{11} , Eq. 6.8;
- 5) SPU calculates the log-normal variance from disc 2, B_{22} , Eq. 6.9;
- 6) SPU calculates the log-normal co-variance, B_{12} , Eq. 6.10;
- 7) Apply saturation correction (if needed) ;
- 8) Calculate the Q factor, Eq. 6.11;
- 9) Derive Cn^2 , Eq. 6.12.

7 Filtering of the data

7.1 Raw Data

LCRD OGS-1' BLS900 is measuring Cn2 values along the approximately horizontal path between the CA Edison tower (Transmitter) and a receiver deployed on the roof of the OCTL telescope.

In this report, we briefly analyze one year worth of data collected by the BLS900, from May 2018 to June 2019 as reported in Fig. 7.1. The sampling/integration rate is one minute. According to the measurements, values of Cn2 can vary from a low value of 3E-18 up to 3E-12 [m^{-2/3}]. Before to analyze in detail the meaning and the physical consequences of the data in Fig. 7.1, it is necessary to point out some irregularities in the data and the need to filter out the set of raw data. There is visible discontinuity in the data when values of Cn2 much larger than 3E-14 up to 5E-12 [m^{-2/3}] are reported. These high(er) Cn2 values appear separated and distinct from the rest of the data: overall, the amount of these data are approximately 2% of data in Fig. 7.1.

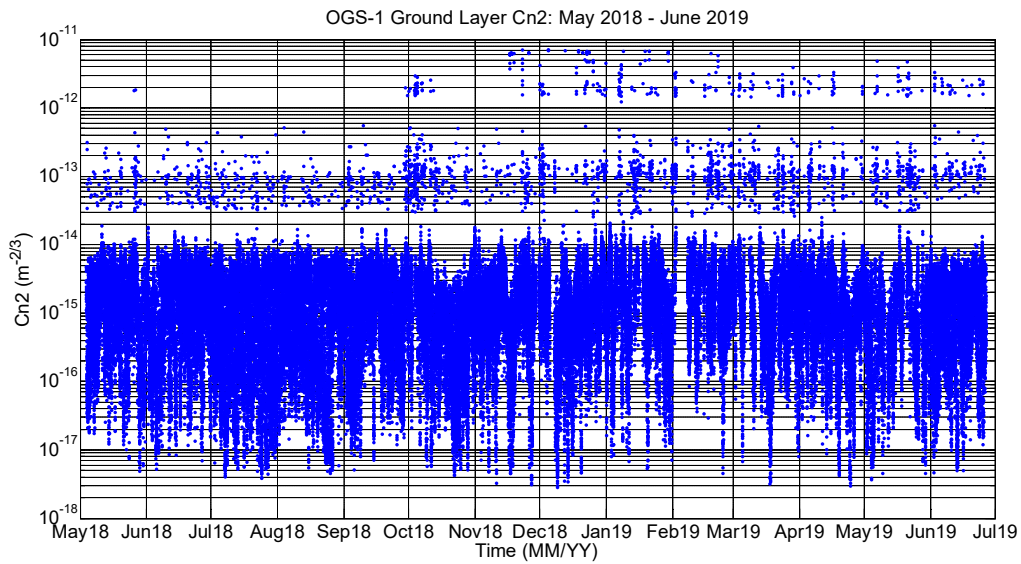


Figure 7.1 Measurements of the coefficient of the structure function of the refractive index (Cn2) at OGS1 as measured by the BLS900. Period: May 2018 to June 2019. There is a number of points of values much larger than 3E-14 up to 5E-12 [m^{-2/3}]. These measurements are considered an artifact of the instrument.

One can speculate that there are a number of reasons to this high value measurement of Cn2, including the presence of inhomogeneity in the transmitter-to-receiver path (fog, rain, etc.), and/or daytime sky radiance that can affect the receiver. To understand the presence of these high Cn2 values, we first isolated these measurements. In other terms, only Cn2 values above $3E-14$ [$m^{-2/3}$] were taken into consideration for the moment. Next, we plotted Cn2 against the Sun zenith angle, Fig. 7.2. The data in Fig. 7.2 indicate that the largest amount of irregular measurements are captured at a Sun zenith angle around 60° and that approximately 40% of these events occur when the Sun zenith angle is larger than 80° (nighttime), indicating that scattering of the sun radiation does not play a role in this problem.

In order to produce a more robust statistics of the data measured, measurements of $Cn2 < 3E-14$ [$m^{-2/3}$] were considered in the subsequent analysis of the data.

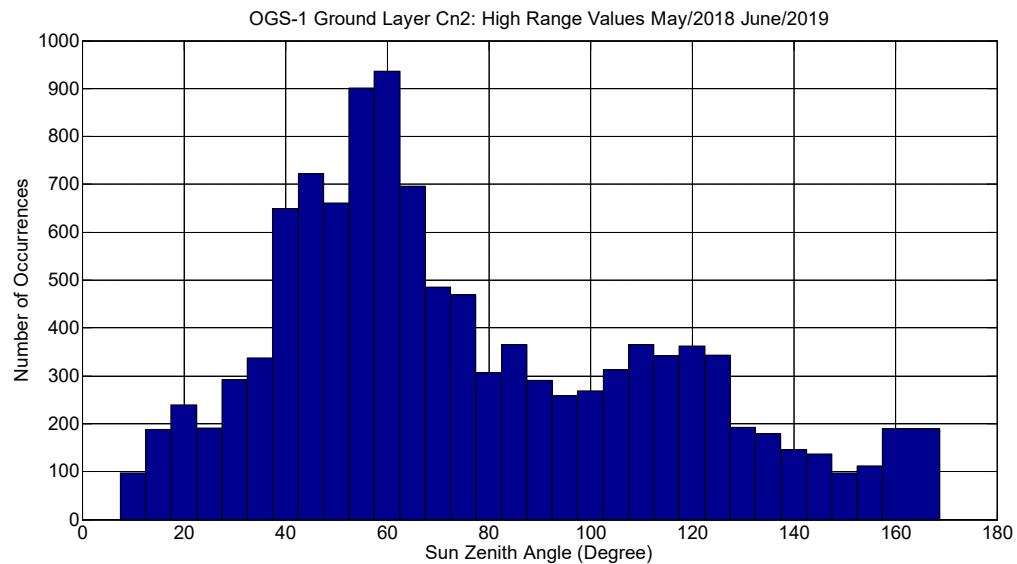


Figure 7.2 Histogram of the occurrences of the high values Cn2 ($Cn2 > 3E-14$) versus Sun zenith angle. The peak is for a relatively large Sun ZA~ 60° .

7.2 First Filtering

After filtering, the range of the Cn₂ values varies from approximately from 4E-18 to 2E-14 [m^{-2/3}], Fig. 7.3. Usually, Cn₂ variations follow a diurnal cycle with the largest Cn₂ values (stronger optical turbulence) around noon, when the Sun zenith angle is the lowest (Sun high in the sky) with a large thermal gradient in the boundary layer of the atmosphere inducing a relatively large coefficient of the atmosphere structure function of the temperature. At the same time, around dawn and sunset one can observe relatively lower Cn₂ values, due to the thermal equilibrium in the atmosphere profile. To illustrate this last concept, Fig. 7.4 presents 3 days of measurements, May 4 2018 to May 7 2018 from the OGS-1 BLS900. Cn₂ measurements are plotted and compared to the variation of the Sun zenith angle (figure below).

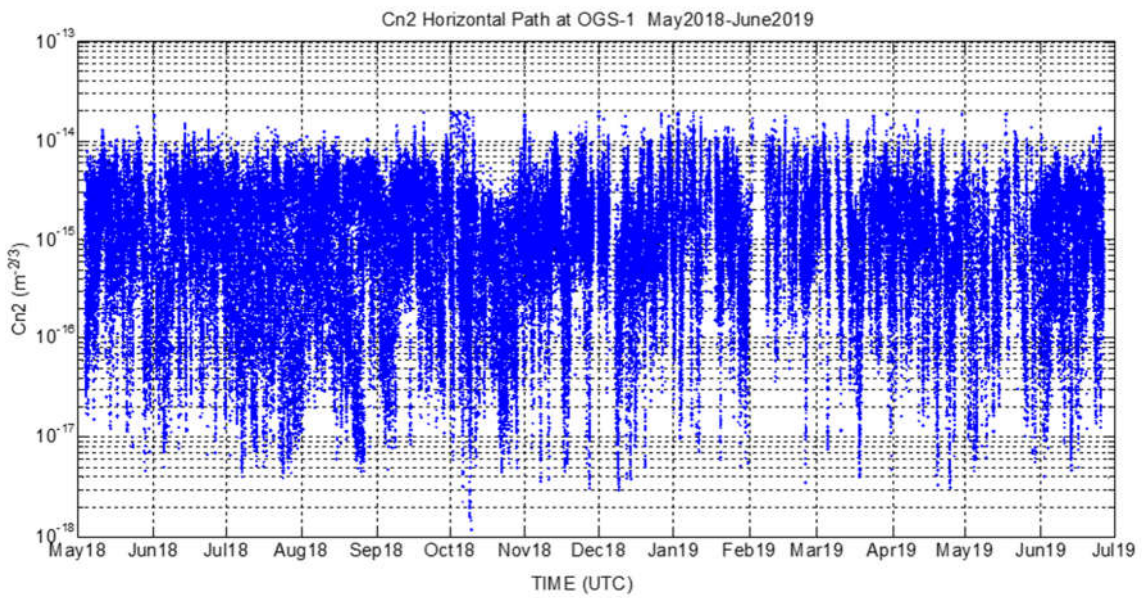


Figure 7.3 Cn₂ values at OGS-1 as measured by the BLS900 after filtering: May 2018 to June 2019.

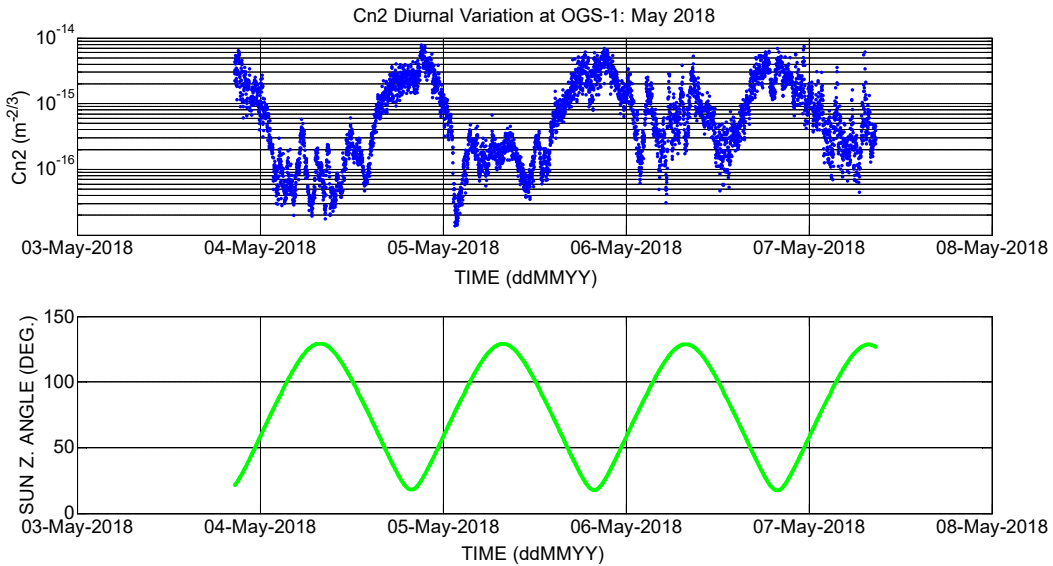


Figure 7.4 Diurnal variation of the turbulence strength ($Cn2$) at OGS-1: Stronger turbulence is observed around noon at lower zenith angle. Turbulence tends to decrease around dawn and sunset. Time is in UTC.

Figure 7.4 noticeably describes the diurnal variation of $Cn2$ respect to the Sun position. During the day, $Cn2$ reaches largest values (between $5E-15$ to $7E-15$ [$m^{-2/3}$]) around noon where the Sun zenith angle is approximately around 25° . The optical turbulence is weaker close to sunset, (Sun zenith angle around 90°) with relatively low values of $Cn2$. After sunset, $Cn2$ values tend to increase and to be stable during the night, with a predisposition to decrease again dawn (again Sun zenith angle of around 90°). One may notice that during the night between May 6 and May 7, $Cn2$ values are relatively large compared to the other nights. This event is not surprising; in fact, a number of other meteorological factors may affect the (nocturnal) variation of $Cn2$, which, however, has always a strong dependence on the Sun position in the sky.

7.3 Sun Zenith Angle dependence

The full year of $Cn2$ measurements is reported in a different fashion (respect to Fig. 7.3) in Fig. 7.5 A. In this last figure $Cn2$ values are reported versus the Sun zenith angle. At the same time, in Fig. 7.5 A and Fig. 7.5 B average and median values of $Cn2$ for a given Sun zenith angle are also indicated (by the red and yellow marker).

At small zenith angle (up to 35 degree approximately), $Cn2$ values have higher average values and median values. At the same time, one can notice that the spread of values that $Cn2$ assumes at low Sun zenith angle is reduced (especially if compared to the nighttime measurements). Moreover, in

this range median and average values are approximately the same, suggesting that statistically the spreading of the values may be represented approximately by a unimodal distribution resembling a ‘Gaussian’ like shape.

Figure 6 depicts a probability density function (pdf) built on the histogram of the values of Cn2 measured when the Sun zenith angle is approximately 20° (daytime, summer). Even if this pdf function appears somehow irregular (probably due to the restricted number of data points available), the derived distribution is clearly unimodal, with some resemblance to a log-normal, with the largest number of events in the range of Cn2 values between 2E-15 to 4E-15 [m^{-2/3}].

Figure 7.7 presents the pdf of Cn2 values when the Sun Zenith angle is 100 degree, 10 degree below the horizon (approximately nighttime condition). Again, the statistics of this figure is built using the yearly dada collected between May 2018 and June 2019 as shown in Fig. 7.5 A. In this case the pdf resemble to a negative exponential statistics, with average Cn2 = 1.2E-15 [m^{-2/3}] and median Cn2 =5E-15 [m^{-2/3}]. The spread of values of Cn2, between mean and the median values is characteristic of negative exponential statistics. From the figure, generally, one can affirm that during nighttime there is a large variation of values of the coefficient of the structure index of the refractive index; however, these values are lower from those what we can observe during daytime when the Sun is relatively high in the sky, Fig. 7.5 A and 7.5 B.

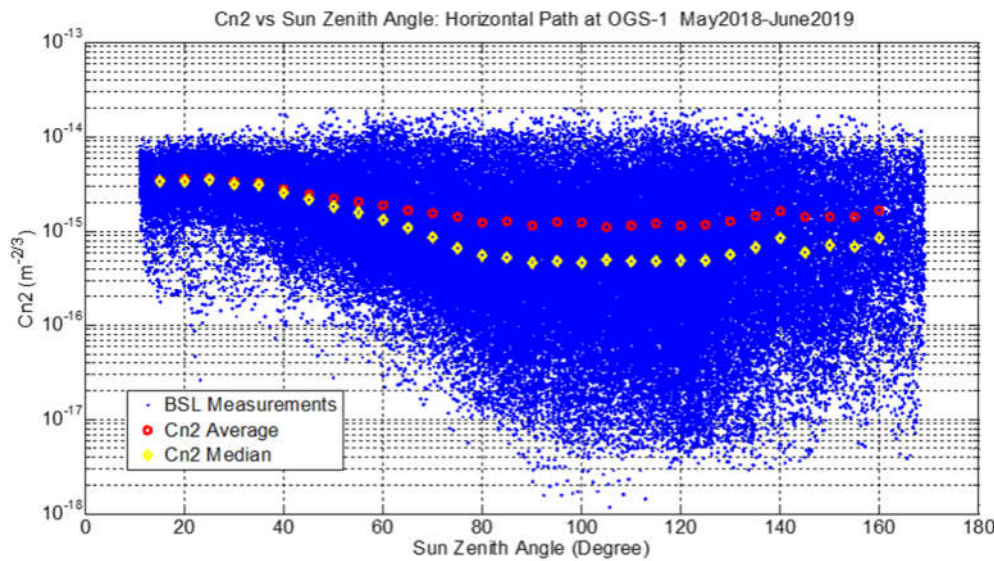


Figure 7.5 A BLS900 measurements of Cn2 at OGS-1 during the period May 2018 –June 2019. Sun Zenith angle is indicated, with larger spread of values for ZA=100°.

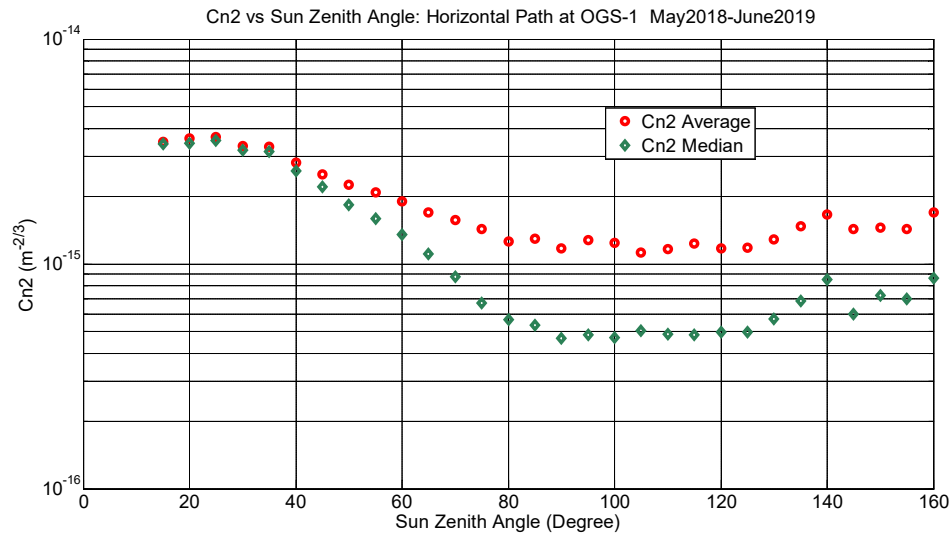


Figure 7.5 B BLS900 measurements of Cn2 at OGS-1 during the period May 2018 –June 2019. Mean and median values of Cn2 versus Sun zenith angle are plotted in the figure.

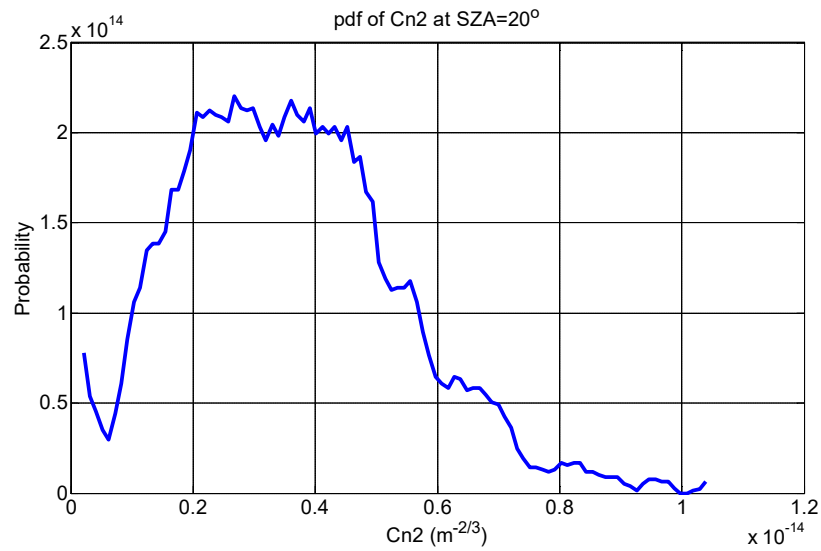


Figure 7.6 Probability distribution function of Cn2 values when the Sun ZA=20°. The curve is obtained from data reported in Fig. 7.5 A.

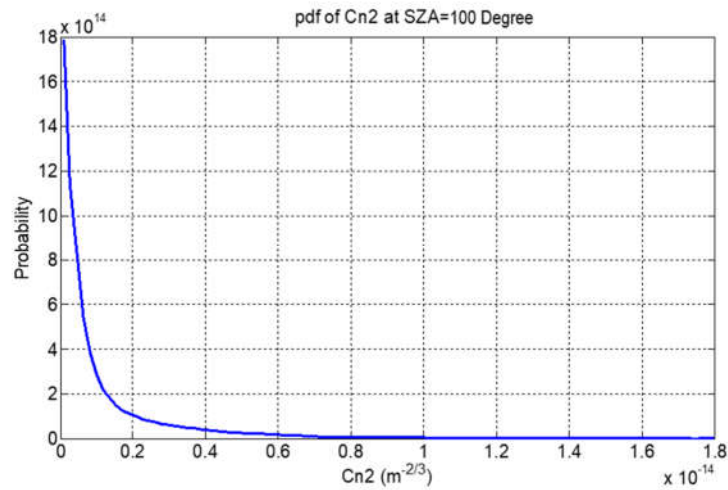


Figure 7.7 Probability distribution function of Cn2 values when the Sun ZA=100° (nighttime).
The curve is obtained from data in Fig. 7.5 A.

7.4 Monthly Variation

Figures 7.8 to 7.19 show the diurnal monthly variation of Cn2 across the valley as measured by the BLS900. To derive the curves in the figures, we used the Cn2 measurements covering the period May 2018 – June 2019 as shown in Fig. 7.3. The plotted diurnal cycles have time scale the local time, where the hour 12:00 corresponds to time when the Sun is highest in the sky. Of course the Sun position at zenith varies according to the season, and consequently we are expecting a different Cn2 values during the months of the year. Median and average diurnal variation of Cn2 are represented in the figures, and one can expect some difference between the curves, according to what described in previous sub-sections and figures appearing in this section of the report.

During the summer months, (June, July, August, September, Fig. 7.13 to 7.16) a distinct Cn2 diurnal cycle is observed: high Cn2 values around noon, with generally lowest Cn2 values around dawn and sunset. During the night hours Cn2 tends to increase respect to the apparent values observed at dawn and sunset. This behaviour is better observed in the diurnal variation of the median (red) curves respect to the average (blue) curves that are always above. Generally, around noon median and average Cn2 value are the same. This observation is in agreement also to what is generally plotted in Fig. 7.5 B.

During the winter months one can observe a totally different Cn2 diurnal cycle from what evinced during the summer months. In December (Fig. 7.19), January and February (Fig. 8, and Fig. 9), a general variation of the Cn2 diurnal cycle cannot be witnessed; moreover the average and the median curves of these months are always separated and distinct: median and average curves do not intersect/touch around noon as observed during the summer months. A number of reasons may be introduced at this moment to explain diurnal cycle of Cn2 during the winter months and why it is dissimilar from what expected/seen during the summer months. First, precipitation and generally bad weather (rain, snow, fog) that is more frequent during the winter can affect the measurements. One should notice that data affected by relatively adverse weather are not filtered out from the set of data here presented. Moreover, the short duration of the daytime combined during winter with the relatively low Sun elevation angle at noon during those months may not contribute to generate dynamic in the thermal profile of the atmosphere that contribute to the distinct Cn2 diurnal cycle during the summer months.

Concerning spring months and fall months one can observe a mixed diurnal behaviour of the Cn2 cycle. During March the diurnal variation of median (not the average) values of Cn2 start resembling to what observed during the summer months, April and May and October definitely have a diurnal cycle of Cn2 approximately similar to what seen during the summer. The diurnal variation of November, Fig. 7.18, is more similar to what observed during the winter months, with distinct median and average curves.

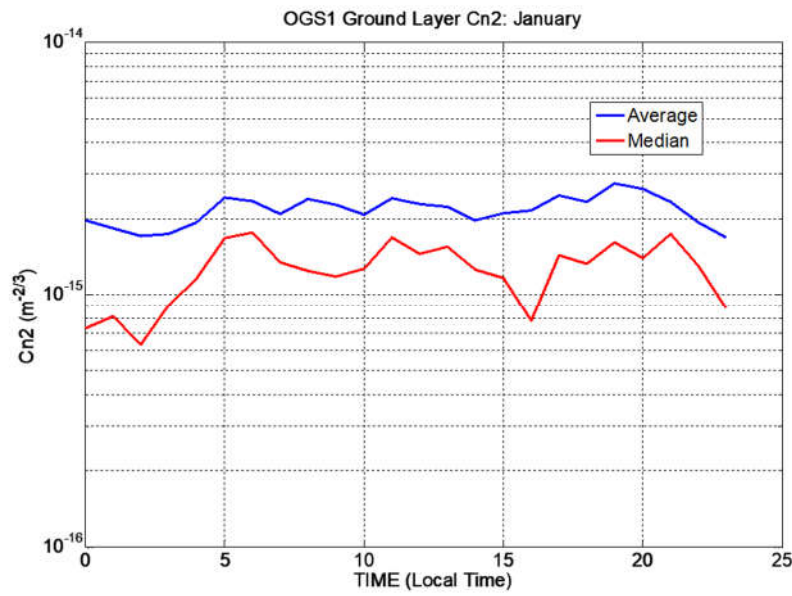


Figure 7.8 Diurnal variation at OGS-1 of Cn2 during the month of January. Curves are obtained by using data in Fig. 7.3: red curve median; blue curve average.

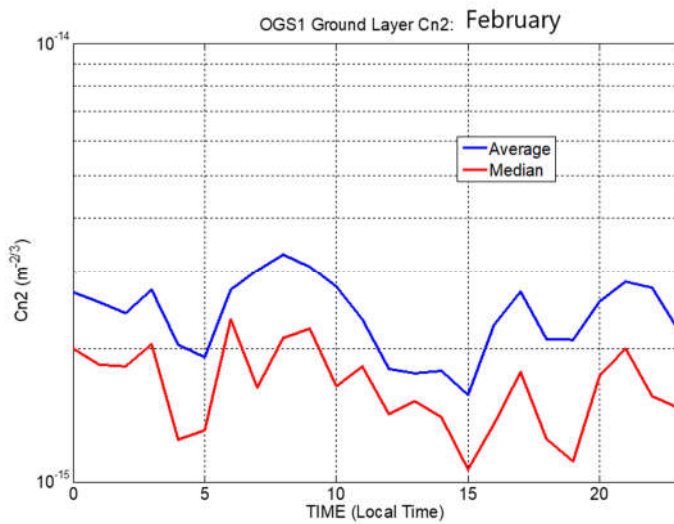


Figure 7.9. Diurnal variation at OGS-1 of Cn2 during the month of February. Curves are obtained by using data in Fig. 7.3: red curve median; blue curve average.

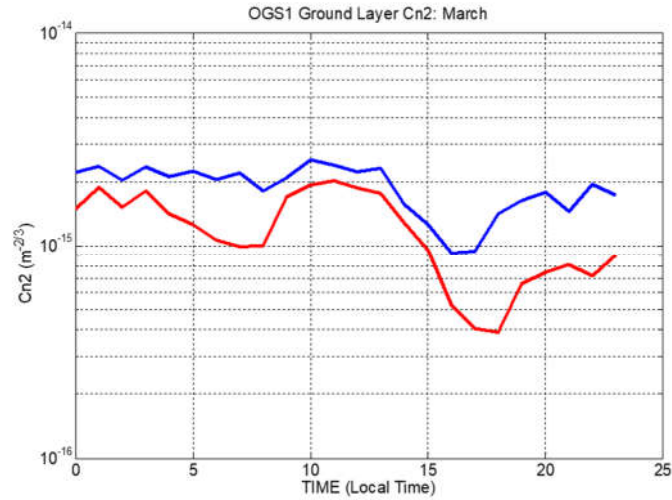


Figure 7.10 Diurnal variation at OGS-1 of C_{n2} during the month of March. Curves are obtained by using data in Fig. 7.3: red curve median; blue curve average.

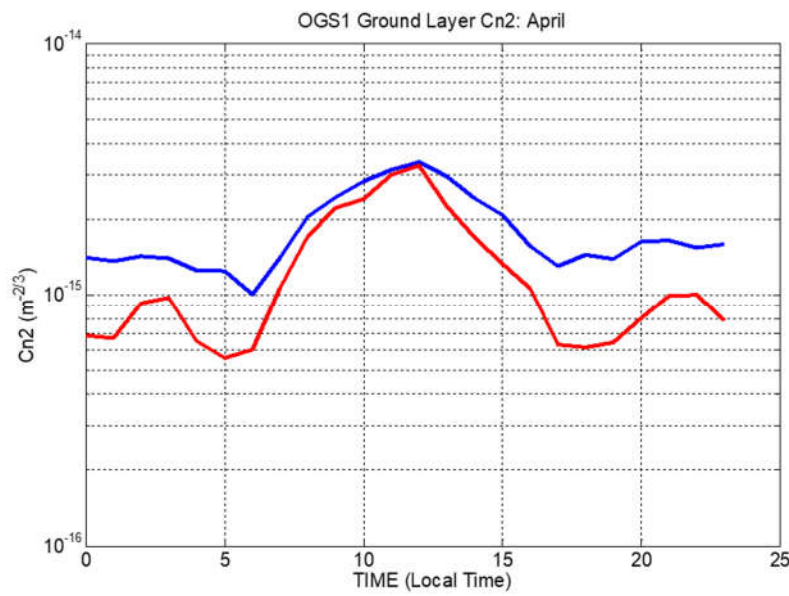


Figure 7.11 Diurnal variation at OGS-1 of C_{n2} during the month of April. Curves are obtained by using data in Fig. 7.3: red curve median; blue curve average.

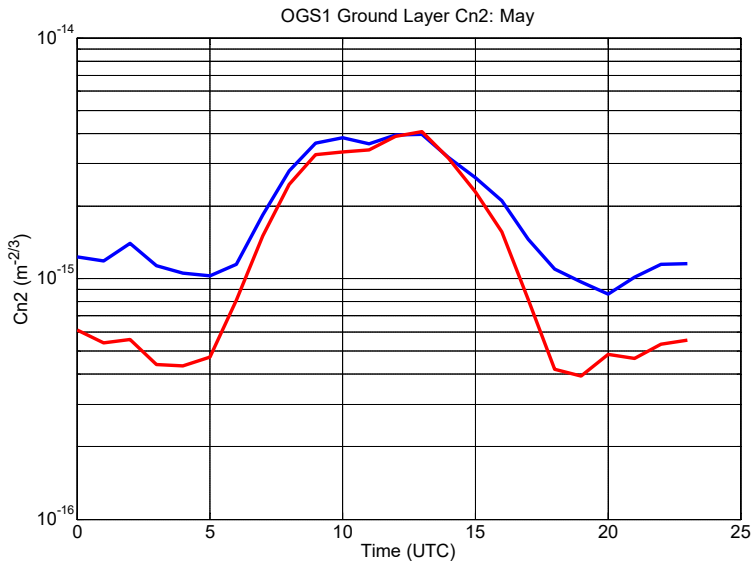


Figure 7.12 Diurnal variation at OGS-1 of Cn2 during the month of May. Curves are obtained by using data in Fig. 7.3: red curve median; blue curve average.

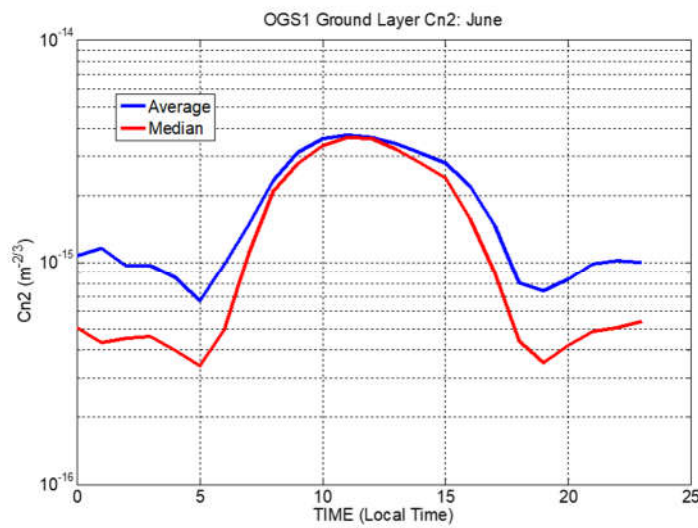


Figure 7.13 Diurnal variation at OGS-1 of Cn2 during the month of June. Curves are obtained by using data in Fig. 7.3: red curve median; blue curve average.

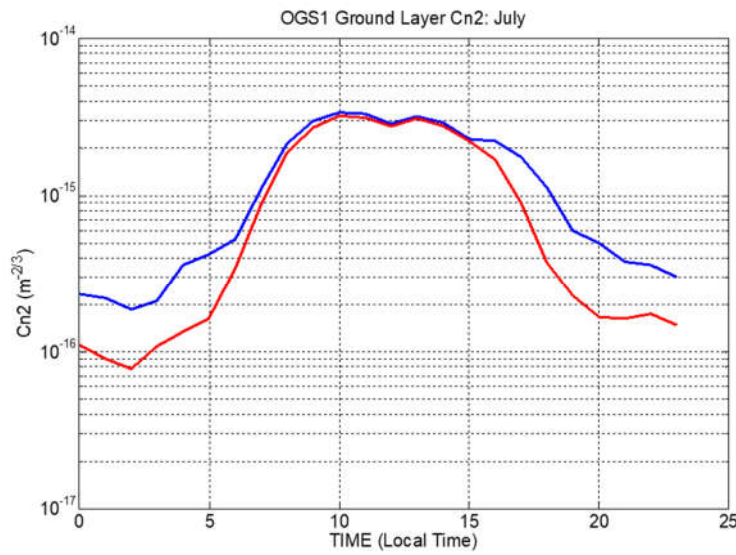


Figure 7.14 Diurnal variation at OGS-1 of C_{n2} during the month of July. Curves are obtained by using data in Fig. 7.3: red curve median; blue curve average.

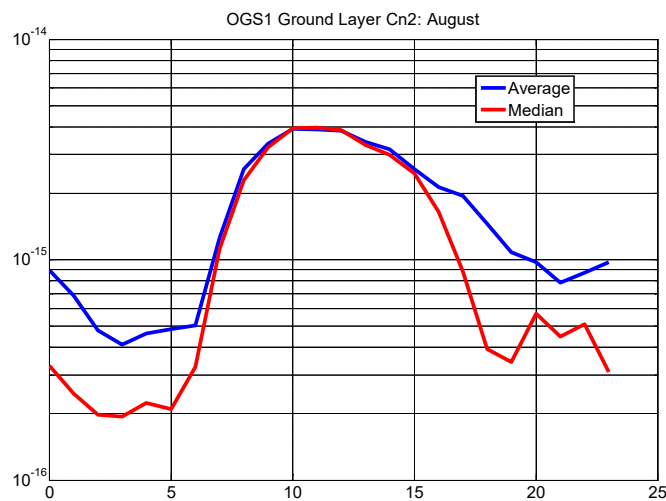


Figure 7.15 Diurnal variation at OGS-1 of C_{n2} during the month of August. Curves are obtained by using data in Fig. 7.3: red curve median; blue curve average.

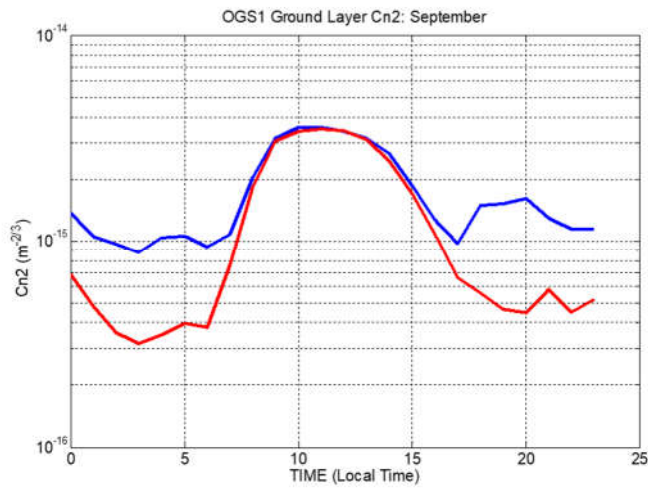


Figure 7.16 Diurnal variation at OGS-1 of Cn₂ during the month of September. Curves are obtained by using data in Fig. 7.3: red curve median; blue curve average.

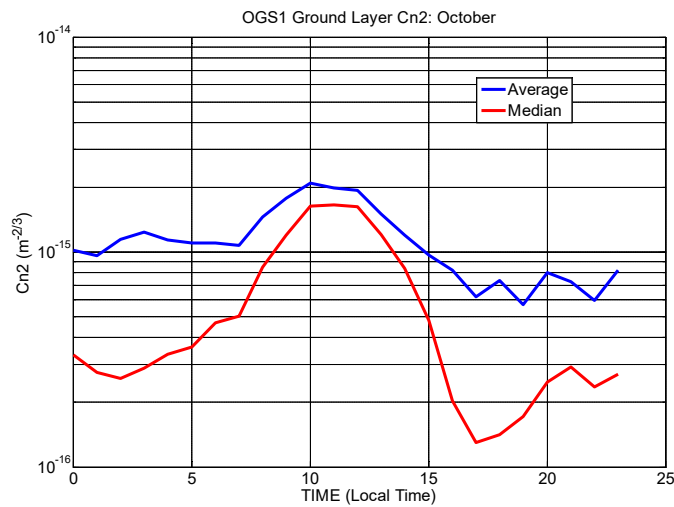


Figure 7.17. Average diurnal variation at OGS-1 of Cn₂ during the month of October. Curves are obtained by using data in Fig. 7.3: red curve median; blue curve average.

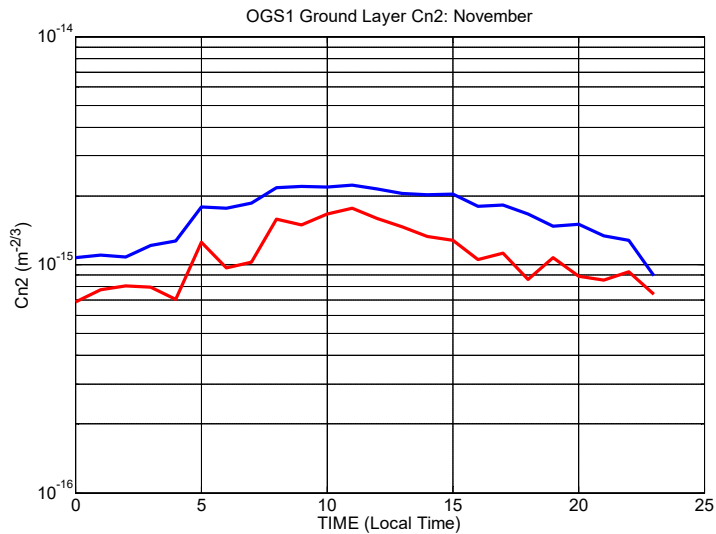


Figure 7.18. Average diurnal variation at OGS-1 of Cn2 during the month of November. Curves are obtained by using data in Fig. 7.3: red curve median; blue curve average.

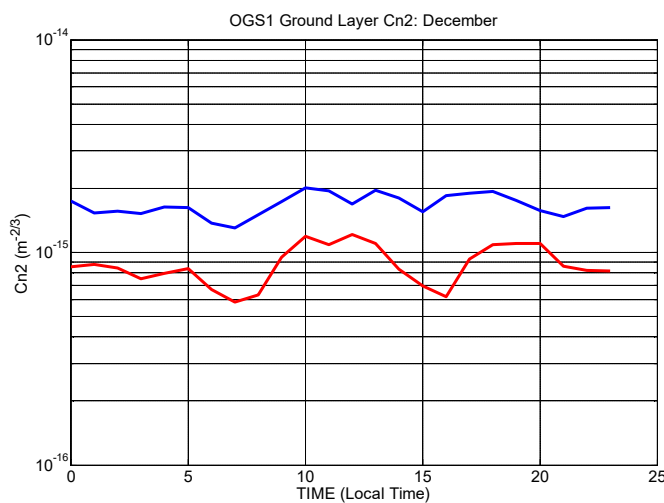


Figure 7.19 Diurnal variation at OGS-1 of Cn2 during the month of December. Curves are obtained by using data in Fig. 7.3; blue curve average.

8 Summary

In this report, we have described the deployment of a boundary layer scintillometer at LCRD's OGS-1 site. The instrument, BLS900 by Scintec AG, provides real time measurements of the coefficient of the structure function of the refractive index as measured (C_{n2}) over a horizontal path of 3.4 Km between transmitter located on the CA Edison tower, a and receiver located across the valley facing the roof the OCTL telescope.

The first part of this report, Sec. 1 to Sec. 5, describes the installation of the hardware and of the software of the instrument, including the technical specification of the BLS900.

A brief theory is also discussed in Sec. 6 to provide the technical background and the principles underlying the instrument operations.

Finally, in last part of this report, Sec. 7, a statistical analysis over one year measured data is proposed. Particularly, the analysis describes the relationship of the optical turbulence strength from Sun zenith angle. Furthermore, a monthly statistics of the diurnal variation of the C_{n2} is also included to illustrate the seasonal variation of diurnal cycle of C_{n2} itself.

9 References

- [1] Scintec Scintillometers: Theory Manual, Version 1.03 (September 2016)
- [2] Scintec Boundary Layer Scintillometer: Installation and Operation Manual, Version 1.03 (September 2016)
- [3] Scintec Surface and Boundary Layer Scintillometer: SRun Software Manual, Version 1.15 (August 2016)
- [4] Scintec BLS Hardware Maintenance Manual
- [5] Scintec Boundary Layer Scintillometer: User Manual, Version 1.49 (December 2008)
- [6] Tatarskii, V.I.: 1961, *Wave propagation in a turbulent medium*. McGraw-Hill Book Company Inc, New York
- [7] Hill, R.J.: 1981, *Saturation resistance and inner-scale resistance of a large-aperture scintillometer - a case-study*, Appl. Opt.
- [8] Hill, R.J. and G.R. Ochs: 1978, Fine calibration of large-aperture optical scintillometers and an optical estimate of inner scale of turbulence, Appl. Opt.
- [9] Wang, T., G.R. Ochs and S.F. Clifford: 1978, *A saturation-resistant optical scintillometer to measure C_{n2}* , J. Opt. Soc. Am. 68